

Microstructure and crystallography of 20MnCr5 steel tempered at different conditions

Shen Cun Wang · Yi Wen Wu · Yi Hua ·
Zhi Cheng Li · Hong Zhang

Received: 29 March 2010 / Accepted: 26 May 2010 / Published online: 20 July 2010
© Springer Science+Business Media, LLC 2010

Abstract The microstructure and crystallography of 20MnCr5 steel tempered at 180 °C for 2 h were examined by electron back scattered diffraction (EBSD) in a field-emission scanning electron microscope. The crystallographic features of martensite in a prior austenite grain area were studied by pole figures (PFs). Compared to the theoretical PFs calculated with Kurdjumow–Sachs (K–S) and Nishiyama–Wassermann (N–W) orientation relationships (ORs), it is shown that both of the ORs exist in the investigated specimens. Misorientations distribution and the result of transmission electron microscope analysis indicating that [011]/54.7° lath boundary existed in the microstructure also prove the coexistence of K–S and N–W ORs. When the steels were further tempered at 350 °C/20 min or 500 °C/20 min, the length of boundaries in equal areas decreased and the crystallographic features still fulfill the coexistence of K–S and N–W ORs.

Introduction

The crystallographic relationship between the second phases and the primary ones in phase transformation is crucial in determining the texture and/or anisotropy of the

final products [1, 2]. Several crystallographic models have been reported to describe the orientation relationships (ORs) of martensite transformation [3–7]. The most frequently referred ones are Kurdjumow–Sachs (K–S) OR $(\langle 111 \rangle_{\gamma} // \langle 110 \rangle_{\alpha}, \langle 1\bar{1}0 \rangle_{\gamma} // \langle \bar{1}\bar{1}1 \rangle_{\alpha})$ [4] and Nishiyama–Wassermann (N–W) OR $(\langle 111 \rangle_{\gamma} // \langle 110 \rangle_{\alpha}, \langle \bar{2}11 \rangle_{\gamma} // \langle \bar{1}\bar{1}0 \rangle_{\alpha})$ [5]. The two relationships only differ from each other by a small relative rotation of 5.26° [8]. The little difference makes them difficult to be discriminated from each other.

The ORs of martensite are conventionally identified by transmission electron microscope (TEM). However, electron back scattered diffraction (EBSD) technique in scanning electron microscope (SEM) has been recently developed to determine the OR of martensite with its prior austenite and many refreshing results have been obtained [9–15]. Martensite in low carbon steel and Fe–28.5%Ni alloy was confirmed to follow K–S and N–W ORs, respectively, by EBSD analysis [11, 12]. The poles in the $\{001\}_{\alpha}$ pole figures (PF) from EBSD examination generally diffuse around the theoretical poles of K–S or N–W OR [11, 12, 14]. The calculated deviation angles between martensite variants' experimental directions and theoretical directions of K–S or N–W OR are generally 6° or smaller [15]. The deviation cannot be attributed to the limitation of angular resolution of EBSD simply. Actually, the diffusion also existed in TEM analysis [16, 17]. Shape strain accommodation mechanism was used to explain the diffusion [18], but arguments still exist.

A kind of software that took the diffusion of experimental poles into consideration was developed by Cayron [19]. By simulating experimental the PFs, they recently proposed for martensite transformation a two-step mechanism that the fcc–bcc transformation results from a fcc–hexagonal close-packed (hcp) step followed by an hcp–bcc step [20]. The mechanism considered that the $\gamma \rightarrow \alpha$

S. C. Wang · Z. C. Li · H. Zhang (✉)
School of Materials Science and Engineering, Central South University, Changsha 410083, Hunan, People's Republic of China
e-mail: hzhang@mail.csu.edu.cn

Y. W. Wu · Y. Hua
Inspection Center of Industrial Products and Raw Materials, Shanghai Entry-Exit Inspection and Quarantine Bureau of the People's Republic of China, Shanghai 200135, People's Republic of China

transformation was a continuous process and the diffusion of experimental data was due to the geometrical trace of transformation history. This needs to be supported by more experimental evidences. Interestingly, Sonderegger et al. [21] combined K–S and N–W ORs and thus explained at least 50–60% of the boundary misorientations of martensite with high precision. The coexistence of K–S and N–W ORs may be reasonable to explain the diffusion of experimental poles.

20MnCr5 (similar to SAE 5120) steel that is widely used in automobile industry [22–24] is a typical low carbon low alloy steel. There is little research concerning its crystallographic features. The steel was studied by EBSD in this paper. An easy method was used to fit the experimental PFs from EBSD results. It was found that the experimental poles also diffused around the theoretical ones. The phenomenon cannot be explained by K–S or N–W OR alone, so the coexistence of K–S and N–W OR is proposed to explain the diffusion. This was also proved by TEM analysis. Besides, the influence of tempering on the crystallographic features of the martensite is systematically studied.

Experimental procedure

The chemical composition (wt%) of the 20MnCr5 steel investigated was 0.23C, 0.02S, 0.015P, 0.089Si, 1.42Mn, 1.21Cr, and balanced Fe. Normalized 20MnCr5 steel was austenitized at 920 °C for 2 h, followed by keeping at 860 °C for 30 min and water quenched to obtain the martensite structure. The quenched steel was tempered at 180 °C for 2 h and then cut into samples with the size of 10 mm × 10 mm × 5 mm. The as-tempered sample was denoted as A. One sample that was further tempered at 350 °C/20 min for three times, each time was followed by cooling in the air for more than 1 h. The sample was denoted as B. The other three samples that were further tempered at 350 °C/20 min for five times, 500 °C/20 min for three times and 500 °C/20 min for five times are denoted as C, D, and E, respectively.

Slices of 0.4–0.5 mm thickness were cut from the treated samples. After being mechanically ground to 0.08–0.1 mm thickness, the slices were punched into disks with diameter of 3 mm. The disks for EBSD analysis were then jet polished with a solution of 5% HClO₄ + C₂H₅OH at –30 °C and a voltage of 36 V. The time for polishing was set to about 40 s to obtain a stress free surface.

The structure of martensite was examined by EBSD/SEM and TEM. EBSD measurements were conducted by a field-emission (FE) scanning electron microscope (Sirion 200) equipped with an EDAX EBSD system. TSL-OIM software was used for the data analysis. The beam scan

mode was selected, the operation voltage was 25 kV and the step size was 200 nm. The TEM observations were carried out on a JEM-2010F operated at 200 kV. The orientation fitting for PFs is programmed with Matlab 7.0.

Results and discussion

The microstructure of the specimen tempered at 180 °C

The as-tempered material (Sample A) develops lath martensite structure that consists of three hierarchies in prior austenite grains [11]: packets, blocks, and laths, as shown in the SEM micrograph in Fig. 1a. The mean size of the prior austenite grains is 12.5 μm. The image quality (IQ) map of sample A from the EBSD measurements over an area of 60 μm × 60 μm is shown in Fig. 1b. The gray-scale of

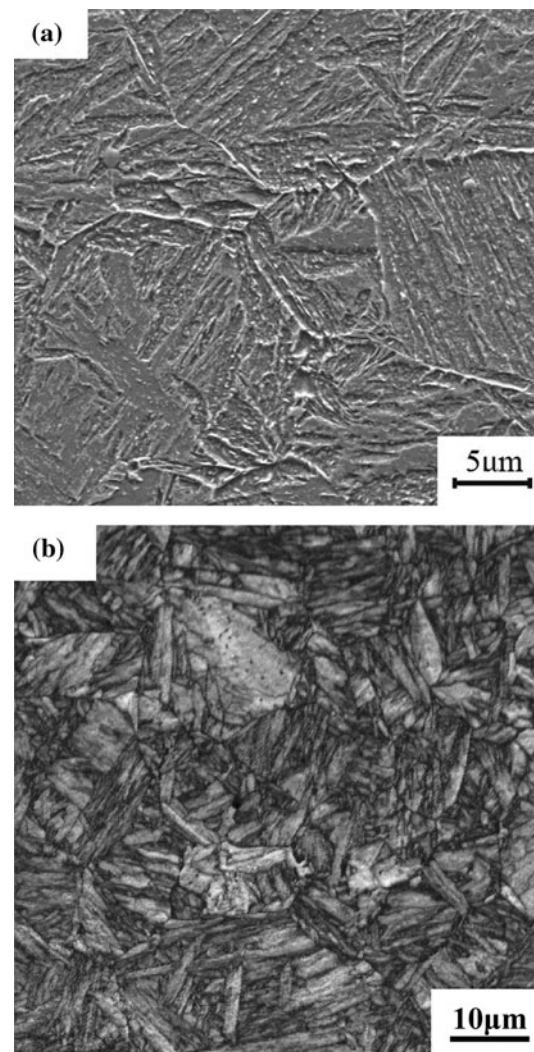
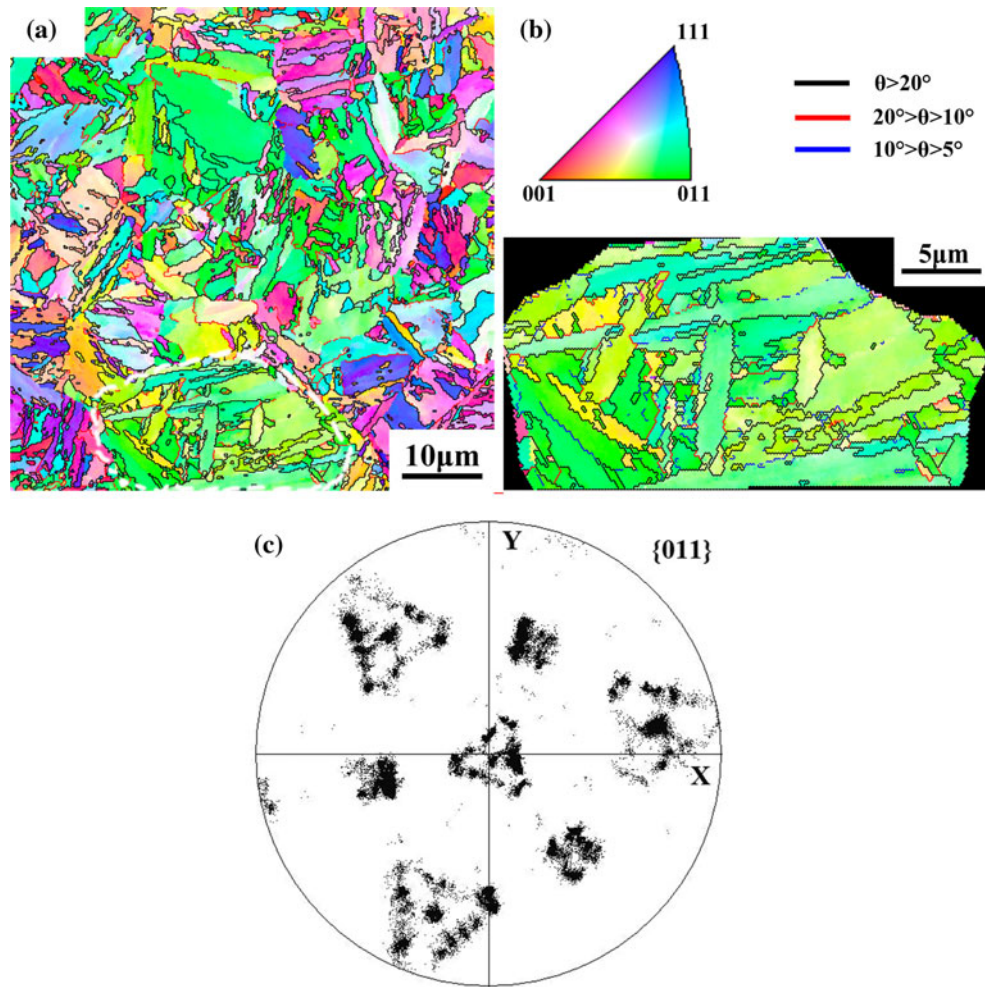


Fig. 1 Microstructure of the lath martensite in Sample A. **a** SEM image and **b** IQ map from EBSD measurement

each point in the map reflects the image quality of the Kikuchi line, which is seriously affected by the distortions and defects. Therefore, grain boundaries and areas with dense defects and distortions are extremely dark. The IQ map clearly reveals a typical lath martensite structure and delineates the prior austenite grain boundaries.

Figure 2a shows the inverse pole figure (IPF) color map of the scanned area, in which the colors correspond to the crystallographic orientation normal to the observed sample plane, as shown in the inset stereographic triangle in Fig. 2b. The color of the whole area in Fig. 2b from Fig. 2a is quite close to green. This indicates that the $\{110\}_{\alpha}$ plane of the area is approximately parallel to the scanned surface according to the stereographic triangle. Grain boundaries with different misorientation angles are drawn in different colors. Most of the boundaries are high angle ones and the misorientation distribution will be described later. The $\{011\}_{\alpha}$ PFs of the area in Fig. 2c are shown in Fig. 2c, in which the poles distributed continuously on four triangular and three square like areas.

Fig. 2 **a** IPF color map of sample A, **b** IPF color map of an area of prior austenite grain circled by white dashed line in (a). Colors of the martensite crystal in (a) and (b) agree with the orientations perpendicular to the observed plane, as indicated in the stereographic triangle in (b). The colors of the grain boundaries correspond to the ranges of misorientation angles in (b). **c** $\{011\}_{\alpha}$ PF of the area in the IPF map (b), respectively



Method for fitting the experimental pole figures

The orientation relationship of martensite with prior austenite in the selected area in Fig. 2b is still unknown. Two probable ORs are K-S and N-W ORs [4, 5]. The 24 variants of K-S OR and 12 variants of N-W OR are listed in Tables 1 and 2.

The change in crystallographic orientations through the martensite transformation can be expressed as

$$\mathbf{M}_i = \mathbf{T}_i \mathbf{A}_i. \quad (1)$$

\mathbf{T}_i is the orientation transformation matrix; \mathbf{M}_i and \mathbf{A}_i are the variant crystallographic orientation matrices for the martensite and austenite, respectively. \mathbf{M}_i and \mathbf{A}_i are composed of three orthogonal unit vectors (crystal direction vector, crystal face vector, and their cross product vector) according to Tables 1 and 2, respectively. For K-S OR, $i = 1, 2, \dots, 24$; for N-W OR, $i = 1, 2, \dots, 12$.

The orientation transformation matrices can then be written as

Table 1 The 24 crystallographic variants for the K–S orientation relationship

Variant	Plane parallel	Direction parallel	Variant	Plane parallel	Direction parallel
V_1	$(111)_\gamma // (011)_\alpha'$	$[\bar{1}01]_\gamma // [\bar{1}\bar{1}1]_{\alpha'}$	V_{13}	$(\bar{1}11)_\gamma // (011)_\alpha'$	$[01\bar{1}]_\gamma // [\bar{1}\bar{1}1]_{\alpha'}$
V_2		$[\bar{1}01]_\gamma // [\bar{1}\bar{1}\bar{1}]_{\alpha'}$	V_{14}		$[01\bar{1}]_\gamma // [\bar{1}\bar{1}\bar{1}]_{\alpha'}$
V_3		$[01\bar{1}]_\gamma // [\bar{1}\bar{1}1]_{\alpha'}$	V_{15}		$[\bar{1}0\bar{1}]_\gamma // [\bar{1}\bar{1}1]_{\alpha'}$
V_4		$[01\bar{1}]_\gamma // [\bar{1}\bar{1}\bar{1}]_{\alpha'}$	V_{16}		$[\bar{1}0\bar{1}]_\gamma // [\bar{1}\bar{1}\bar{1}]_{\alpha'}$
V_5		$[\bar{1}\bar{1}0]_\gamma // [\bar{1}\bar{1}1]_{\alpha'}$	V_{17}		$[110]_\gamma // [\bar{1}\bar{1}1]_{\alpha'}$
V_6		$[\bar{1}\bar{1}0]_\gamma // [\bar{1}\bar{1}\bar{1}]_{\alpha'}$	V_{18}		$[110]_\gamma // [\bar{1}\bar{1}\bar{1}]_{\alpha'}$
V_7	$(1\bar{1}1)_\gamma // (011)_\alpha'$	$[\bar{1}0\bar{1}]_\gamma // [\bar{1}\bar{1}1]_{\alpha'}$	V_{19}	$(1\bar{1}\bar{1})_\gamma // (011)_\alpha'$	$[\bar{1}10]_\gamma // [\bar{1}\bar{1}1]_{\alpha'}$
V_8		$[\bar{1}0\bar{1}]_\gamma // [\bar{1}\bar{1}\bar{1}]_{\alpha'}$	V_{20}		$[\bar{1}10]_\gamma // [\bar{1}\bar{1}\bar{1}]_{\alpha'}$
V_9		$[\bar{1}\bar{1}0]_\gamma // [\bar{1}\bar{1}1]_{\alpha'}$	V_{21}		$[01\bar{1}]_\gamma // [\bar{1}\bar{1}1]_{\alpha'}$
V_{10}		$[\bar{1}\bar{1}0]_\gamma // [\bar{1}\bar{1}\bar{1}]_{\alpha'}$	V_{22}		$[01\bar{1}]_\gamma // [\bar{1}\bar{1}\bar{1}]_{\alpha'}$
V_{11}		$[011]_\gamma // [\bar{1}\bar{1}1]_{\alpha'}$	V_{23}		$[101]_\gamma // [\bar{1}\bar{1}1]_{\alpha'}$
V_{12}		$[011]_\gamma // [\bar{1}\bar{1}\bar{1}]_{\alpha'}$	V_{24}		$[101]_\gamma // [\bar{1}\bar{1}\bar{1}]_{\alpha'}$

Table 2 The 12 crystallographic variants for the N–W orientation relationship

Variant	Plane parallel	Direction parallel	Variant	Plane parallel	Direction parallel
V_1	$(111)_\gamma // (011)_\alpha'$	$[2\bar{1}\bar{1}]_\gamma // [0\bar{1}1]_{\alpha'}$	V_7	$(\bar{1}11)_\gamma // (011)_\alpha'$	$[21\bar{1}]_\gamma // [0\bar{1}1]_{\alpha'}$
V_2		$[\bar{1}2\bar{1}]_\gamma // [0\bar{1}1]_{\alpha'}$	V_8		$[\bar{1}\bar{2}\bar{1}]_\gamma // [0\bar{1}1]_{\alpha'}$
V_3		$[\bar{1}\bar{1}2]_\gamma // [0\bar{1}1]_{\alpha'}$	V_9		$[\bar{1}\bar{1}2]_\gamma // [0\bar{1}1]_{\alpha'}$
V_4	$(1\bar{1}1)_\gamma // (011)_\alpha'$	$[\bar{2}\bar{1}\bar{1}]_\gamma // [0\bar{1}1]_{\alpha'}$	V_{10}	$(1\bar{1}\bar{1})_\gamma // (011)_\alpha'$	$[2\bar{1}\bar{1}]_\gamma // [0\bar{1}1]_{\alpha'}$
V_5		$[\bar{1}2\bar{1}]_\gamma // [0\bar{1}1]_{\alpha'}$	V_{11}		$[\bar{1}\bar{2}\bar{1}]_\gamma // [0\bar{1}1]_{\alpha'}$
V_6		$[\bar{1}\bar{1}2]_\gamma // [0\bar{1}1]_{\alpha'}$	V_{12}		$[2\bar{1}\bar{1}]_\gamma // [0\bar{1}1]_{\alpha'}$

$$\mathbf{T}_i = \mathbf{M} \mathbf{A}_i^{-1}. \quad (2)$$

$\{001\}_\alpha$ PFs were used to study the crystallographic features of martensite in former studies [11, 12]. However, since $(111)_\gamma // (011)_\alpha$ in both of the ORs, the $\{011\}_\alpha$ PFs can indicate the relationship between martensite and prior austenite more directly. This can be seen later. In calculating the theoretical $\{011\}_\alpha$ PFs, the unit cell of martensite is considered to be cubic rather than tetragonal. The consideration is to simplify the calculation, as done in former studies in the literatures [11, 12]. Due to cubic symmetry, there are six identical $\{011\}_\alpha$ faces in martensite unit cell. They constitute the matrix \mathbf{F}_{011}

$$\mathbf{F}_{011} = \begin{pmatrix} 1 & 1 & 0 & \bar{1} & 1 & 0 \\ 1 & 0 & 1 & 1 & 0 & \bar{1} \\ 0 & 1 & 1 & 0 & \bar{1} & 1 \end{pmatrix}$$

\mathbf{F}_{011} should be transformed to $(111)_\gamma[1\bar{1}0]_\gamma$ coordinate system by the rotation matrix \mathbf{T}_c :

$$\mathbf{T}_c = \begin{pmatrix} 1 & 1 & 1 \\ 1 & \bar{1} & 1 \\ \frac{1}{2} & 0 & 1 \end{pmatrix}^{-1}$$

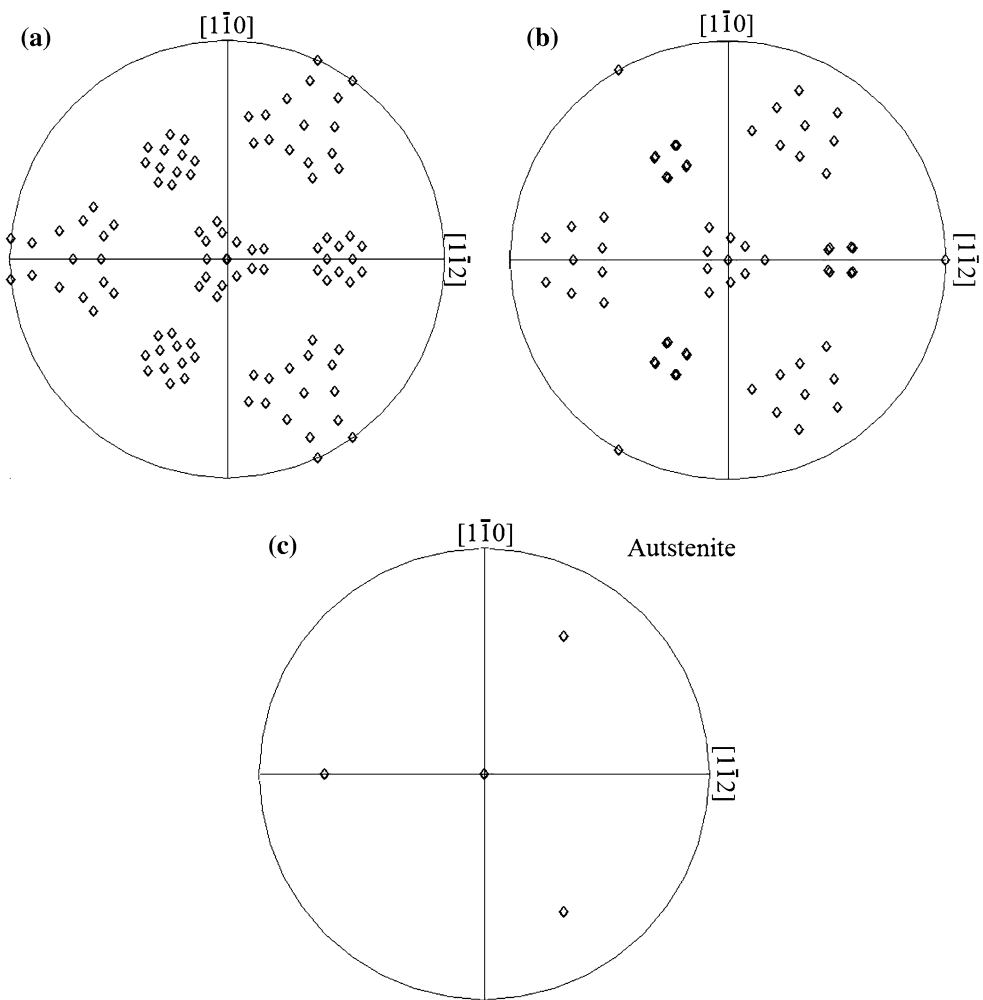
\mathbf{T}_c and \mathbf{T}_i need to be normalized. The $\{011\}_\alpha$ face direction vectors of martensite variants in austenite $(111)_\gamma[1\bar{1}0]_\gamma$ coordinate system can be calculated by

$$\mathbf{V}_i = \mathbf{T}_c \mathbf{T}_i^{-1} \mathbf{F}_{011} \quad (3)$$

The $\{011\}_\alpha$ PFs of K–S and N–W ORs can be drawn from \mathbf{V}_i by stereographic projection. The results are shown in Fig. 3a, b, respectively. Each PF is composed of three near square groups and four near triangular groups. The center poles of the triangular shape groups are found to coincide with the four $\{111\}_\gamma$ poles of the standard austenite $\{111\}_\gamma$ PF with $(111)_\gamma[1\bar{1}0]_\gamma$ orientation (Fig. 3c). The coincidence of poles means the $\{011\}_\alpha$ are parallel to $\{111\}_\gamma$. This relationship is the key in fitting the experimental PFs and make $\{011\}_\alpha$ PFs fitted more accurately than $\{001\}_\alpha$ PFs.

The coordinate of the center points of two adjacent triangular shape groups in Fig. 2c are measured to be (x_0, y_0) and (x_3, y_3) . The orientation vectors of the two points can then be calculated to be $[a_0, b_0, c_0]$ and $[a_3, b_3, c_3]$ by the stereographic projection rule. According to the relationship mentioned earlier, it can be assumed that $[a_0, b_0, c_0] // [1\bar{1}\bar{1}]$ and $[a_3, b_3, c_3] // [111]$, since the $\{111\}_\gamma$ are identical. It is set that $[a_1, b_1, c_1] = [a_0, b_0, c_0] \times [a_3, b_3, c_3]$, $[a_2, b_2, c_2] = [a_3, b_3, c_3] \times [a_1, b_1, c_1]$. Since $[1\bar{1}\bar{1}] \times [111] = [1\bar{1}0]$ and $[111] \times [1\bar{1}0] = [11\bar{2}]$, it is obvious that $[a_1, b_1, c_1] // [1\bar{1}0]$, $[a_2, b_2, c_2] // [11\bar{2}]$. Therefore, the rotation matrix from austenite $(111)_\gamma[1\bar{1}0]_\gamma$ system to sample coordinate system is \mathbf{T}_s

Fig. 3 $\{011\}_x$ PF showing the poles of the martensite variants transformed from a single crystal austenite with $(111)_\gamma[1\bar{1}0]_\gamma$ orientation that maintain the K–S (a) and N–W (b) ORs. c Standard austenite $\{111\}_\gamma$ PFs with $(111)_\gamma[1\bar{1}0]_\gamma$ orientation



$$\mathbf{T}_s = \begin{pmatrix} a_1 & a_2 & a_3 \\ b_1 & b_2 & b_3 \\ c_1 & c_2 & c_3 \end{pmatrix}$$

After normalization, \mathbf{T}_s can be used to calculate the fitted PFs by

$$\mathbf{V}_i = \mathbf{T}_s \mathbf{T}_c \mathbf{T}_i^{-1} \mathbf{F}_{011}. \quad (4)$$

Here, \mathbf{V}_i is the orientation vectors of $\{011\}_x$ faces in the sample coordinate system. By adjusting the measured (x_0, y_0) and (x_3, y_3) , the best fitted PFs can be obtained.

The $\{011\}_x$ PF in Fig. 2c was fitted following the above procedure and was superimposed with the calculated theoretical poles of K–S or N–W OR, as shown by the diamond symbols in Fig. 4a, b, respectively. It can be found that experimental poles diffuse around the theoretical ones of K–S or N–W OR, and distribute continuously between the adjacent theoretical directions. But there are still small pole clusters in the PFs. By comparing Fig. 4a, b, it is easy to find that most of the poles of N–W OR locate at the

center of the clusters, while the poles of K–S OR lie around the edges (see the areas marked with A and B in the figures). This indicates that the N–W OR fits the OR of 20MnCr5 martensite with prior austenite more accurately than the K–S OR. The deviation of experimental directions from N–W OR is 6° or smaller [10], so it is not sufficient to conclude the experimental OR by N–W OR alone. Since poles of K–S OR also coincide with a part of the experimental poles, it is considered that K–S OR also exists in practical 20MnCr5 tempered martensite, but the OR of the martensite follows mainly the N–W OR.

Kitahara et al. [11] and Morito et al. [14] reported that martensite in low carbon low alloy steel follows K–S OR, which is inconsistent with our results. Actually, their demonstrations were based on the assumption that the martensite steel used in their study followed K–S OR, to confirm the OR. The experimental poles of $\{001\}_x$ PFs also diffuse around the calculated K–S OR poles in their results, but they did not consider other probable ORs such as N–W OR. Both of the ORs are considered in our study and it is

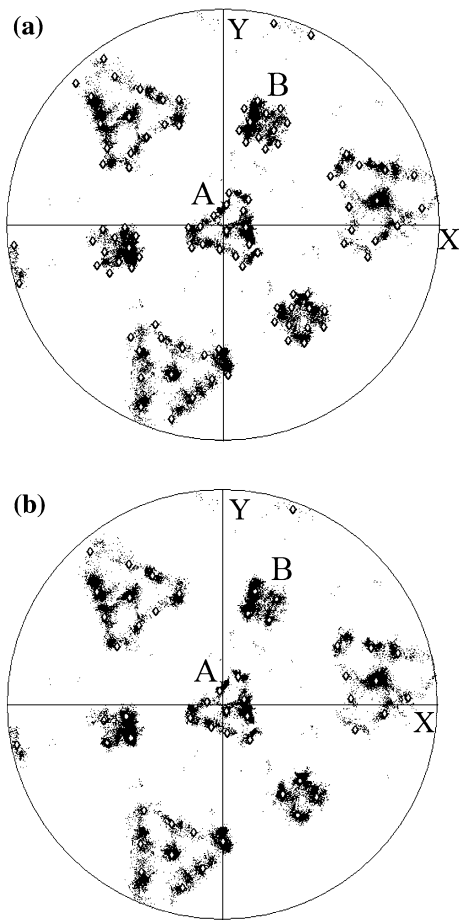


Fig. 4 $\{011\}_\alpha$ PFs in Fig. 2c superimposed with poles of K-S (a) or N-W (b) variants

found that martensite in 20MnCr5 steel mostly follows N-W OR. More facts are given in the following.

The orientation distribution in the tempered (180°C) specimen

The distribution of misorientation angles between adjacent points of the selected area in Fig. 2b is illustrated in Fig. 5. Misorientations that are smaller than 3° are not drawn, so that the details of the distribution could be more evident. Two main groups of misorientation angles are visible in the distribution curve: one with misorientations smaller than 20° and another with misorientations from 45° to 62° . The peak at 60° is extremely high, which indicates that most of the high angle boundaries are close to 60° .

According to the calculation by Gourgues et al. [25], the theoretical misorientation between two martensite variants formed from the same austenite grain with K-S and/or N-W ORs are shown in Table 3. All the misorientations in Table 3 can be found in Fig. 5, but the misorientations are not distributed discretely on the calculated values. If one of the two

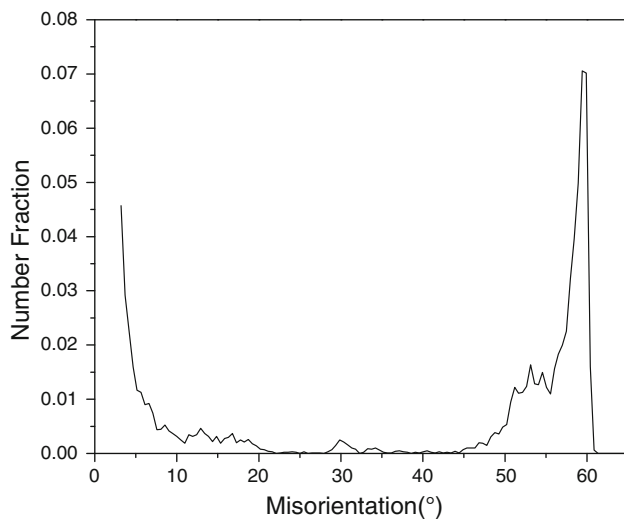


Fig. 5 Distribution of misorientation angles between adjacent martensite points of the area in Fig. 2b

ORs is assumed for real martensite, most of the misorientations in the distribution curve cannot be explained. However, if both of them were assumed to exist in the martensite, there will be 25 different values of misorientations that fit the misorientation distribution curve with smaller intervals. This is another evidence of the coexistence of K-S and N-W ORs.

TEM observation of the lath structure

Figure 6a shows a bright-field TEM image of the lath martensite in the 20MnCr5 steel. Composite selected area electron diffraction (SAED) pattern of the two adjacent laths marked with M_1 and M_2 in Fig. 6a is shown in Fig. 6b. They can be indexed as $B/[1\bar{1}\bar{1}]_{M_1}//[001]_{M_2}$. The two laths have a common parallel plane $(011)_{M_1}//(011)_{M_2}$. The misorientation between the two laths is calculated to be 54.7° .

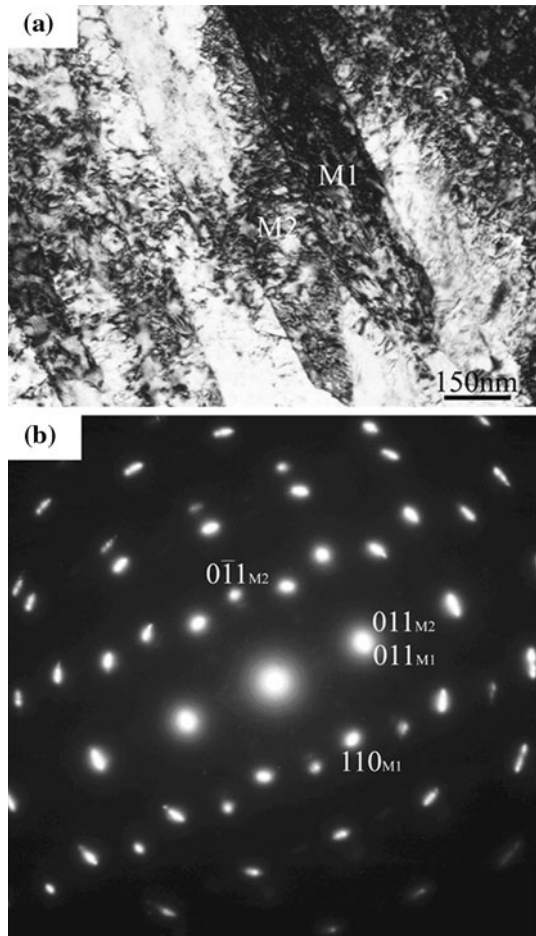
The misorientation value 54.7° only exists in the group of K-S/N-W variants that formed from the same $\{111\}_\gamma$ (see in Table 3). This accurately proves that both K-S and N-W ORs exist in 20MnCr5 martensite. The K-S and N-W variants cannot be distinguished, because no retained austenite exists. So it is assumed that M_1 is an N-W variant and M_2 is a K-S variant. The orientation relationship between M_1 and M_2 is schematically shown in Fig. 7. They share the common plane $(011)_\alpha$ with 54.7° boundary. This kind of boundary is also observed by other researchers [26, 27]. The result of TEM examination also proved the coexistence of K-S and N-W ORs.

EBSM observation of specimens tempered at different conditions

Figure 8a shows the IQ index distribution curves of samples A, C, and E. The peaks of the curves move towards

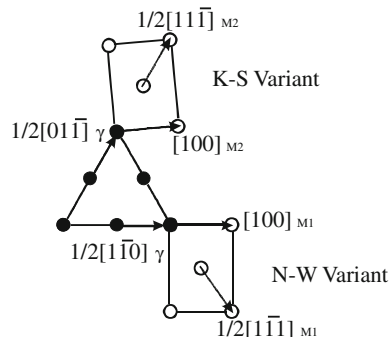
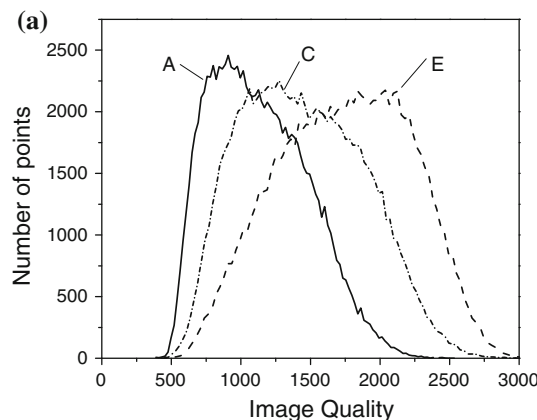
Table 3 Misorientation of variants calculated from K-S and N-W OR (degree)

	Same $\{111\}_\gamma$	Two different $\{111\}_\gamma$
K-S/K-S	0, 60, 49.5	10.5, 14.9, 20.6, 21.1, 47.1, 49.5, 50.5, 51.7, 57.2
N-W/N-W	0, 60	13.8, 19.5, 50.5, 53.7
K-S/N/W	5.26, 54.7, 60.2	11.8, 17.2, 20.2, 48.6, 50.9, 52.1, 55.7, 58.8

**Fig. 6** **a** A bright-field TEM image of the lath martensite in the 20MnCr5 steel. **b** Composite SAED pattern of two variants of martensite laths marked with M_1 and M_2

higher IQ index with the increase of tempering temperature. The increase of IQ index indicates that the density of defects and distortion decreased. The image quality map of sample E is given to exhibit the influence of tempering on the microstructure (Fig. 8b).

The IPF color maps over areas of $60 \mu\text{m} \times 60 \mu\text{m}$ in the 20MnCr5 steel tempered at $350^\circ\text{C}/20\text{ min}$ or $500^\circ\text{C}/20\text{ min}$ for various times are exhibited in Fig. 9. The areas in the figures encircled with white dashed lines are chosen to study their crystallographic structure in detail. These figures exhibit the lath structure of martensite, and many polygonal grains appear in Fig. 9d.

**Fig. 7** Schematic draw of $[011]/54.7^\circ$ lath relationship by one K-S variant and one N-W variant from the same prior austenite $(111)_\gamma$ plane**Fig. 8** **a** Distribution of IQ index of sample A, C, and E. **b** IQ map of sample E

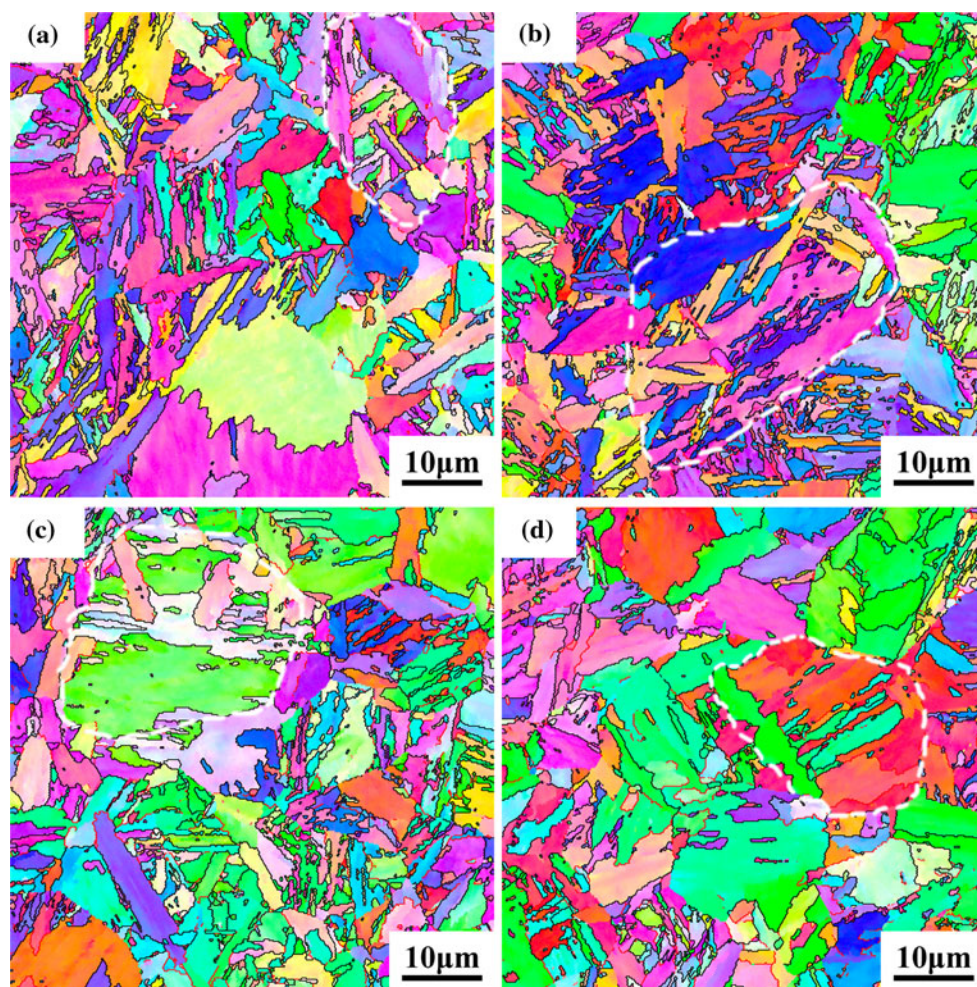


Fig. 9 IPF color map of martensite in the 20MnCr5 steel tempered at different conditions. **a** Sample B. **b** Sample C. **c** Sample D. **d** Sample E

Table 4 Length of boundaries with different misorientation angles (mm)

Material state	Rotation angle intervals of boundaries			
	2°–5°	5°–20°	20°–45°	45°–62°
Sample A (length of boundaries)	3.15 ± 0.33	1.52 ± 0.18	0.51 ± 0.14	4.78 ± 0.63
Sample B (length of boundaries)	2.58 ± 0.70	1.10 ± 0.40	0.26 ± 0.12	3.62 ± 1.24
Sample C (length of boundaries)	2.24 ± 0.30	1.20 ± 0.17	0.28 ± 0.14	4.53 ± 0.65
Sample D (length of boundaries)	2.23 ± 0.30	1.21 ± 0.27	0.34 ± 0.15	3.87 ± 0.69
Sample E (length of boundaries)	1.61 ± 0.28	1.13 ± 0.30	0.38 ± 0.16	3.05 ± 0.64

The length of grain boundaries with rotation angles in four intervals from 2° to 62° is listed in Table 4. The length of boundaries in the interval of 2°–5° decreased continuously. The decrease of low angle boundaries is mainly caused by the decrease of dislocation when tempering. Similar result is obtained by TEM analysis [28]. The length of grain boundaries in the scanned area of samples B, C, D, and E in the interval of 5°–20° and 20°–45° are quite

smaller than sample A, but they do not show much difference from each other. The length of high angle grain boundaries (HAGB) with misorientations between 45° and 62° of the samples also decreased with the increase of tempering temperature and time. HAGB are generally proved to be difficult to migrate at low temperature such as 350 °C [29, 30]. However, EBSD technique with high accuracy seems to reveal the little decrease. The decrease

means that HAGB are also influenced by tempering at 350 °C. The reason is still unknown. The length of HAGB in sample B is extremely low. It is easy to see that two large grains at the downside of the IPF map of sample B do not have boundaries larger than 10°. The standard deviations of grain boundary length of sample B are extremely larger than others. The heterogeneity of the grain sizes leads to the exception of sample B.

In Fig. 9, the orientation of the whole scanned area distributed randomly for samples B, C, D, and E. Local areas (encircled with white dashed lines in Fig. 9) that might be transformed from prior austenite grains are selected to obtain their $\{011\}_\alpha$ PFs (see in Fig. 10). The PFs of prior austenite grain areas in samples B, C, D, and E are fitted by N–W OR, and superimposed by theoretical poles according to N–W OR, following the designed procedure. Compared with Fig. 4, the PFs in Fig. 10 do not exhibit obvious difference. The orientation relationship still follows mainly N–W OR, and the spread of practical poles means K–S OR also exist in the 20MnCr5 steel tempered at 350 °C or 500 °C (K–S OR is not drawn in the pole figures).

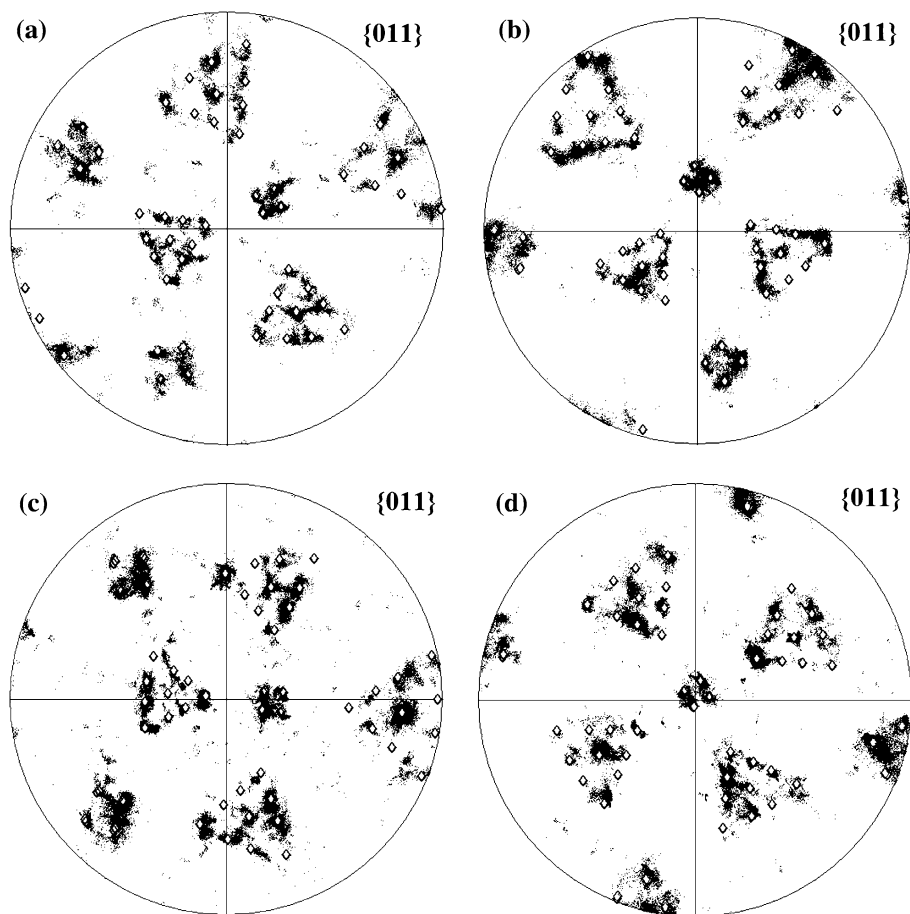
Conclusions

The microstructures and crystallography of tempered martensite in 20MnCr5 steel with different tempering conditions were investigated by EBSD in FE-SEM and TEM.

The IQ map from EBSD can clearly reveal the steel's typical lath martensite structure and delineate the prior austenite grain boundaries. The poles on $\{011\}_\alpha$ PFs distributed continuously on four triangular and three square like areas. The diffusion of experimental poles around the theoretical poles indicated that both K–S and N–W orientation relationships exist in the martensite, but the orientation relationship of the martensite follows mainly the N–W orientation relationship.

The coexistence of K–S and N–W orientation relationships explained the distribution of misorientations with small intervals. TEM observation found the existence of [011]/54.7° lath boundary which can only be formed by adjacent K–S variant and N–W variant transformed from the same $(111)_\gamma$ plane. This confirmed the coexistence of martensite maintaining both K–S and N–W orientation relationships.

Fig. 10 PFs of martensite in the selected prior austenite areas in Fig. 9. The figures are superimposed with theoretical poles of N–W OR as the diamonds. **a** Sample B. **b** Sample C. **c** Sample D. **d** Sample E



The length of both low angle and high angle grain boundaries decreased with the increase of tempering temperature and times. The orientation relationship in the areas transformed from prior austenite grains in the samples tempered at 350 °C/20 min or 500 °C/20 min still followed the coexistence of K–S and N–W orientation relationships.

Acknowledgements This work was supported by the National Natural Science Foundation of China (50872155), the national specific research of public quality sector (2007GYJ028) and China Postdoctoral Science Foundation.

References

1. Xu YB, Yu YM, Xiao BL, Liu ZY, Wang D (2009) J Mater Sci 44:3928. doi:[10.1007/s10853-009-3526-4](https://doi.org/10.1007/s10853-009-3526-4)
2. Das D, Chattopadhyay PP (2009) J Mater Sci 44:2957. doi:[10.1007/s10853-009-3392-0](https://doi.org/10.1007/s10853-009-3392-0)
3. Bain EC (1924) Trans Metall Soc AIME 70:25
4. Kurdjumov GV, Sachs GZ (1930) Z Phys 64:325
5. Nishiyama Z (1934) Sci Rep Tohoku Imp Univ Tokyo 23:637
6. Greninger AB, Troiano ARJ (1949) Met Trans 185:590
7. Pond RC, Ma X, Hirth JP (2008) J Mater Sci 43:3881. doi:[10.1007/s10853-007-2158-9](https://doi.org/10.1007/s10853-007-2158-9)
8. Headley TJ, Brooks JA (2002) Metall Trans A 33A:5
9. Gourgues-Lorenzon AF (2007) Int Mater Rev 52:65
10. Bohn T, Bruder E, Muller C (2008) J Mater Sci 43:7307. doi:[10.1007/s10853-008-2682-2](https://doi.org/10.1007/s10853-008-2682-2)
11. Kitahara H, Ueji R, Tsuji N, Minamino Y (2006) Acta Mater 54:1279
12. Kitahara H, Ueji R, Ueda M, Minamino Y (2005) Mater Charact 54:378
13. Calliari I, Brunelli K, Zanellato M, Ramous E, Bertelli R (2009) J Mater Sci 44:3764. doi:[10.1007/s10853-009-3505-9](https://doi.org/10.1007/s10853-009-3505-9)
14. Morito S, Tanaka H, Konishi R, Furuhara T, Maki T (2003) Acta Mater 51:789
15. Adachi Y, Hakata K, Tsuzaki K (2005) Mater Sci Eng A 412:252
16. Zhang MX, Kelly PM (2006) Mater Sci Eng A 438–440:272
17. Zhang MX, Kelly PM (1998) Acta Mater 46:4081
18. Miyamoto G, Takayama N, Furuhara T (2009) Scripta Mater 60:1113
19. Cayron C (2007) Appl Cryst 40:1179
20. Cayron C, Barcelo F, Carlan Y (2010) Acta Mater 58:1395
21. Sonderegger B, Mitsche S, Cerjak H (2007) Mater Charact 58:874
22. Rentsch R (2009) Mat-wiss u Werkstofftech 40:374
23. Barnett MR, Balasubramanian R, Kumar V, MacRae C (2009) J Mater Sci 44:2192. doi:[10.1007/s10853-008-3007-1](https://doi.org/10.1007/s10853-008-3007-1)
24. dos Santos CN, Vieira AG, Paula AS, Viana CSC (2009) J Mater Sci 44:3057. doi:[10.1007/s10853-009-3405-z](https://doi.org/10.1007/s10853-009-3405-z)
25. Gourgues AF, Flower HM, Lindley TC (2000) Mater Sci Technol 16:26
26. Wei FG, Tsuzaki K (2005) Acta Mater 53:2419
27. Rao BVN (1979) Metall Trans A 10:645
28. Pešićka J, Dronhofer A, Eggeler G (2004) Mater Sci Eng A 387–389:176
29. Song SH, Faulkner RG, Flewitt PEJ (2000) Mater Sci Eng A 1–2:23
30. Samuel FH, Hussein AA (1982) Metallography 15(4):391